Numerical Investigation of the Evolution of Vortex Instability in a 2-D Compressible Flow over a Cylinder

Axel Rohde
Department of Aerospace Engineering
Embry-Riddle Aeronautical University
Daytona Beach, Florida 32114

This paper presents a computational fluid dynamics (CFD) study of 2-D flow over a cylinder at a Mach number of 0.3 and diameter based Reynolds numbers ranging between 50 and 1000. The flow simulation was marched in time from an impulsive start and reveals the evolution of vortex instability. After the cylinder has traveled between 100 and 1000 diameters, alternate vortex shedding begins, and a von Karman vortex street develops in the wake. Throughout the initial transient of the flow, the lift coefficient shows periodic oscillation with steady amplitude growth rates from machine precision until periodic vortex shedding is reached, and a distinct frequency shift is observed at the onset of vortex shedding at higher Reynolds numbers. The numerical algorithm is based on a finite volume description of the unsteady, compressible Navier Stokes equations. The inviscid subset of the equations is modeled according to the total variation diminishing (TVD) principle with the numerical viscosity control parameter set to zero. No turbulence modeling was implemented, since the flow is below the transition Reynolds number of 300,000. The accuracy of the scheme is second order in space and first order in time.

Nomenclature

a	=	speed of sound
$\vec{a}$	=	eigenflux component system
$\vec{b}$	=	eigenflux component system
c_p	=	specific heat at constant pressure
c_v	=	specific heat at constant volume
C_D	=	drag force coefficient
C_L	=	lift force coefficient
dA	=	differential area
dV	=	differential volume
D	=	cylinder diameter
e	=	internal energy per unit mass
e_k	=	kinetic energy per unit mass
e_o	=	stagnation energy per unit mass
f_D	=	frequency of periodic drag
f_L	=	frequency of periodic lift
$\vec{f}$	=	force per unit area vector
$\bar{f}$	=	eigenflux system
$\bar{F}$	=	flux system
g_L	=	exponential growth rate of lift
$\vec{g}$	=	flux correction system
h	=	enthalpy per unit mass

h_o	=	stagnation enthalpy per unit mass
$\bar{l}$	=	non-dimensional eigenvalue system
$\bar{L}$	=	left eigenvector
$\bar{\bar{L}}$	=	matrix of left eigenvectors
$\vec{m}$	=	numerical viscosity modifier system
M	=	Mach number
$\hat{n}$	=	unit normal vector
$\vec{n}$	=	numerical viscosity modifier system
p	=	pressure
$\vec{q}$	=	heat flux vector
$\bar{Q}$	=	flow system
R	=	gas constant
$\vec{R}$	=	right eigenvector
$\bar{\bar{R}}$	=	matrix of right eigenvectors
Re	=	Reynolds number
St	=	Strouhal number
t	=	time
T	=	temperature
u, v	=	Cartesian velocity components
$\vec{u}$	=	flux correction system
$\vec{v}$	=	velocity vector
V_∞	=	wind speed

American Institute of Aeronautics and Astronautics

x, y	=	Cartesian coordinates				

I. Introduction

The flow over a circular cylinder has been studied for well over a century, dating back to early experiments by Strouhal, Lord Rayleigh, and von Karman [1-3]. Cylinder flow has seen widespread attention throughout the twentieth century due to its many industrial applications, such as flow over antennas, power lines, chimneys, off-shore risers, and virtually any cylindrical structure subject to strong currents or high winds. In the last three decades many computational fluid dynamics (CFD) studies have focused on cylinder flow, as it is a fairly simple model to set up, and computed results can readily be compared with experimental studies [4-7]. More recently, CFD researchers have revisited the cylinder to investigate the mechanisms of flow instability and have explored methods to suppress certain instability modes [8-10].

A number of instability modes have been identified with cylinder flow associated with its wake, separated shear layer, boundary layer, and three-dimensional instabilities along its span [11-13]. Each mode adds a time varying component to the flow and can generally be observed above a critical Reynolds number (*Re*). The primary wake instability develops around *Re* = 47. For *Re* < 47, the flow is steady and two-dimensional with a symmetric vortex on each side of the wake center line. Above *Re* = 47, the vortex pair starts to wobble, and periodic vortex shedding sets in around *Re* = 65, forming the well known von Karman vortex street. Around *Re* = 200 the flow slowly loses its two-dimensional character as vortex deformation sets in along the span of the cylinder. Between 300 < *Re* < 1000, the separated shear layers undergo a Kelvin-Helmholtz instability, which slowly breaks up the structure of the vortex street in the downstream wake. The location of the breakup point moves upstream with increasing Reynolds number. Around *Re* = 200,000, the boundary layer near the surface of the cylinder transitions from laminar to turbulent, the vortex periodicity starts to disappear, and above *Re* = 350,000 the wake becomes fully turbulent.

II. Recent Work

Experimentalists have only been able to identify instability boundaries within a broad range of Reynolds numbers, especially for higher Reynolds number flows. CFD researchers are now trying to pinpoint the instability thresholds to exact Reynolds numbers by narrowing their range. Rather than simulating a flow directly to find the stability cut-off points of certain modes, which is computationally rather expensive, the more recent numerical work relies on global stability analysis, which is based on linearized perturbation theory and can be summarized as follows: A perturbed time varying flow is expressed as the sum of its steady and unsteady components. The unsteady component or disturbance is written in exponential form through an unknown complex parameter with real and imaginary parts.

The sign of the real part will determine whether a disturbance will grow or decay over time, whereas the imaginary part will determine its frequency. By substituting these linearized perturbation equations into the governing flow equations and subtracting the steady component, the complex parameter becomes an eigenvalue of the resulting system and can be solved numerically subject to the boundary conditions of the flow. The computed eigenvalue with the largest real part corresponds to the primary instability of the flow, and its imaginary part is the frequency through which the disturbance periodically grows over time. Such numerical eigenvalue analysis has recently been applied to a number of flow problems to find global stability limits, where the cylinder problem generally served as a benchmark test [10,13,14].

III. Problem Statement

The precise developmental origin of the primary wake instability above $Re = 47$ and the subsequent onset of vortex shedding appear not to be entirely understood judging from the review of even the most recent literature. Experimentalists attributed this wake instability to the fact that any physical flow can hardly be kept free from upstream low level turbulence or small cross-flow disturbances due to the finite cylinder length [7,15]. Early CFD research speculated that the Navier Stokes equations may have two solutions near the critical Reynolds number, depending on the initial flow conditions [4]. Later CFD research concluded that the Navier-Stokes equations are inherently unstable above $Re = 47$, due to a Hopf bifurcation point, yet fails to show an example of a flow simulation transitioning from steady to unsteady state without numerically disturbing the flow to initiate vortex shedding [5,8,11]. This raises the question of how small upstream flow disturbances could be to still trigger wake instability above $Re = 47$. Can these disturbances be quantified in terms of a turbulence intensity level, and can they result in growth rates and growth frequencies predicted by linear perturbation theory?

IV. Solution Overview

In the present work, a direct numerical prediction of the unsteady flow is obtained using a numerical algorithm based on the finite-volume description of the unsteady, compressible Navier-Stokes equations. The numerical scheme is formally second-order accurate in space and first-order accurate in time. The inviscid subset of the equations is modeled according to the total variation diminishing (TVD) principle with the numerical viscosity parameter set to zero [16-25]. This feature preserves the natural formation of the viscous boundary layer and wake flows at Mach numbers $M \geq 0.3$ very well, but at the same time it makes the present formulation inadequate for incompressible flow predictions $(M = 0)$. The current version of the code has been applied to simulate a 2-D flow over a cylinder at a Mach number $M = 0.3$ and diameter-based Reynolds numbers of $Re = 50, 60, 65, 70, 100, 1000$. No turbulence modeling was implemented for these cases, since the flow is far below the transitional Reynolds number of 300,000. The simulation is carried out in a computational domain extending 15 cylinder diameters away from the boundary, on a mesh with resolutions ranging from 200×150 to 400×250. In the following sections, the governing equations, numerical method, and their implementation are discussed in detail.

V. Governing Equations

The unsteady Navier-Stokes equations, representing a system of conservation equations for mass, momentum, and energy in a viscous flow, can be written in vector notation as the sum of a volume and surface integral,

$$\frac{\partial}{\partial t} \int_{CV} \bar{Q}\, dV \;+\; \oint_{CS} \bar{F}\, dA \;=\; 0 \tag{1}$$

where, for two-dimensional problems,

$$\bar{Q} = \begin{bmatrix} \rho \\ \rho u \\ \rho v \\ \rho e_o \end{bmatrix}, \qquad \bar{F} = \begin{bmatrix} \rho v_n \\ \rho u v_n - f_x \\ \rho v v_n - f_y \\ \rho h_o v_n - e_n \end{bmatrix} \tag{2}$$

and,

$$v_n = \vec{v} \cdot \hat{n} = u n_x + v n_y \tag{3}$$

$$n_x^2 + n_y^2 = 1$$

The stagnation energy and enthalpy per unit mass are defined as the sum of static and dynamic parts, respectively,

$$e_o = e + e_k , \qquad h_o = h + e_k \tag{4}$$

$$e_k = \tfrac{1}{2}\left(u^2 + v^2 \right)$$

with e_k being the kinetic energy per unit mass. Static energy, enthalpy, and pressure can all be expressed in terms of the local speed of sound a, a function of temperature, and the ratio of specific heats γ,

$$e = \frac{a^2}{\gamma(\gamma-1)} , \qquad h = \frac{a^2}{\gamma-1} , \qquad p = \frac{\rho a^2}{\gamma} \tag{5}$$

where,

$$a^2 = \gamma R T , \qquad \gamma = c_p / c_v \tag{6}$$

The energy flux e_n across a cell boundary, which is due to heat exchange as well the work done by the viscous stress tensor, is defined as follows,

$$e_n = \left(\vec{\vec{\tau}} \cdot \vec{v} - \vec{q} \right) \cdot \hat{n} \tag{7}$$

where,

$$\vec{\vec{\tau}} = \begin{bmatrix} \tau_{xx} & \tau_{xy} \\ \tau_{yx} & \tau_{yy} \end{bmatrix}, \qquad \vec{q} = \begin{pmatrix} q_x \\ q_y \end{pmatrix} \tag{8}$$

The force per unit area vector $\vec{f}$, which appears in the momentum equation, is the dot product of the stress tensor $\vec{\vec{\sigma}}$ and the outward unit normal to the local cell surface,

$$\vec{f} = \vec{\vec{\sigma}} \cdot \hat{n} = \begin{pmatrix} f_x \\ f_y \end{pmatrix} \tag{9}$$

where,

$$\vec{\vec{\sigma}} = \begin{bmatrix} \tau_{xx} - p & \tau_{xy} \\ \tau_{yx} & \tau_{yy} - p \end{bmatrix} \tag{10}$$

The components of the viscous stress tensor $\vec{\vec{\tau}}$, based on a Cartesian frame of reference, are determined through local velocity gradients,

$$\tau_{xx} = \frac{2}{3}\mu\left(2\frac{\partial u}{\partial x} - \frac{\partial v}{\partial y}\right)$$

$$\tau_{xy} = \mu\left(\frac{\partial v}{\partial x} + \frac{\partial u}{\partial y}\right) = \tau_{yx} \tag{11}$$

$$\tau_{yy} = \frac{2}{3}\mu\left(2\frac{\partial v}{\partial y} - \frac{\partial u}{\partial x}\right)$$

Similarly, the components of the heat flux vector $\vec{q}$ are determined through local temperature gradients according to Fourier's law of heat conduction,

$$q_x = -\kappa\,\frac{\partial T}{\partial x}\,, \qquad q_y = -\kappa\,\frac{\partial T}{\partial y} \tag{12}$$

VI. Numerical Method

In the applied numerical formulation, the Navier-Stokes equations are discretized and solved in time using first-order accurate explicit time marching. At each time level, the physical fluxes ($\bar{F}$) are summed over all four faces of the 2-D finite volume elements. A set of corrective eigenfluxes ($\bar{f}$), closely tied to the eigensystem of the inviscid Euler equations, is further added to the discretized equations in order to assure stability of the numerical scheme. Note that their presence renders the overall discretization total variation diminishing (TVD). Denoting the spatial locations with subscript indices and time levels with superscript indices, the discretized equations become,

$$\bar{Q}_{i,j}^{p+1} = \bar{Q}_{i,j}^{p} - \frac{\Delta t}{\Delta V_{i,j}}\left\{\left(\bar{F}_{i+1/2,j}\,\Delta A_{i+1/2,j} + \bar{F}_{i,j+1/2}\,\Delta A_{i,j+1/2}\right)\right.$$
$$\left. - \left(\bar{F}_{i-1/2,j}\,\Delta A_{i-1/2,j} + \bar{F}_{i,j-1/2}\,\Delta A_{i,j-1/2}\right)\right\} \tag{13}$$
$$+ \frac{1}{2}\left\{\left(\bar{f}_{i+1/2,j} + \bar{f}_{i,j+1/2}\right) - \left(\bar{f}_{i-1/2,j} + \bar{f}_{i,j-1/2}\right)\right\}$$

where,

$$\bar{F}_{i+1/2,j} = \tfrac{1}{2}\bar{F}(\bar{Q}_{i,j}^{p}) + \tfrac{1}{2}\bar{F}(\bar{Q}_{i+1,j}^{p})$$

$$\bar{F}_{i-1/2,j} = \tfrac{1}{2}\bar{F}(\bar{Q}_{i,j}^{p}) + \tfrac{1}{2}\bar{F}(\bar{Q}_{i-1,j}^{p}) \tag{14}$$

The eigenfluxes are constructed according to Harten's [16] original TVD scheme, with one significant modification: instead of using the numerical viscosity function of the form,

$$\text{Viscos}(x) = \begin{cases} \frac{1}{2}\left(x^2/\varepsilon + \varepsilon\right) & \text{if } |x| \le \varepsilon \\ |x| & \text{if } |x| > \varepsilon \end{cases} \tag{15}$$

$$0 < \varepsilon \le 0.5$$

the absolute value function, $\text{Abs}(x) = |x|$, was used in all successive formulas. Such practice is equivalent to setting the numerical viscosity parameter $\varepsilon = 0$. Thus, one obtains,

$$\bar{f}_{i+1/2,j} = \bar{\bar{R}}_{i+1/2,j} \cdot \bar{b}_{i+1/2,j}$$

(16)

$$\bar{\bar{R}}_{i+1/2,j} = \bar{\bar{R}}(\bar{Q}^p_{i+1/2,j}) , \quad \bar{Q}^p_{i+1/2,j} = \frac{1}{2}\left(\bar{Q}^p_{i,j} + \bar{Q}^p_{i+1,j}\right)$$

$$\bar{b}_{i+1/2,j} = \mathrm{Abs}\left(\bar{l}_{i+1/2,j} + \bar{m}_{i+1/2,j}\right)\bar{a}_{i+1/2,j} - \left(\bar{u}_{i,j} + \bar{u}_{i+1,j}\right)$$

(17)

$$\bar{a}_{i+1/2,j} = \bar{\bar{L}}_{i+1/2,j} \cdot \Delta\bar{Q}^p_{i+1/2,j}$$

(18)

$$\Delta\bar{Q}^p_{i+1/2,j} = \bar{Q}^p_{i+1,j} - \bar{Q}^p_{i,j} , \quad \bar{\bar{L}}_{i+1/2,j} = \bar{\bar{L}}(\bar{Q}^p_{i+1/2,j})$$

where $\bar{\bar{R}}$ and $\bar{\bar{L}}$ are the matrices of the right and left eigenvectors of the Euler equations in the normal vector format,

$$\bar{\bar{R}} = \begin{bmatrix} 1 & 1 & 1 & 0 \\ u-an_x & u & u+an_x & n_y \\ v-an_y & v & v+an_y & -n_x \\ h_o-av_n & e_k & h_o+av_n & un_y-vn_x \end{bmatrix}$$

(19)

$$\bar{\bar{L}} = \begin{bmatrix} \dfrac{(\gamma-1)e_k+av_n}{2a^2} & \dfrac{(1-\gamma)u-an_x}{2a^2} & \dfrac{(1-\gamma)v-an_y}{2a^2} & \dfrac{\gamma-1}{2a^2} \\[2ex] \dfrac{a^2-(\gamma-1)e_k}{a^2} & \dfrac{(\gamma-1)u}{a^2} & \dfrac{(\gamma-1)v}{a^2} & \dfrac{1-\gamma}{a^2} \\[2ex] \dfrac{(\gamma-1)e_k-av_n}{2a^2} & \dfrac{(1-\gamma)u+an_x}{2a^2} & \dfrac{(1-\gamma)v+an_y}{2a^2} & \dfrac{\gamma-1}{2a^2} \\[2ex] vn_x-un_y & n_y & -n_x & 0 \end{bmatrix}$$

(20)

The flux correction terms $\bar{u}$ and $\bar{m}$ are calculated based on the Minmod flux limiter function,

$$\begin{aligned} \bar{m}_{i+1/2,j} &= \left(\bar{u}_{i+1,j} - \bar{u}_{i,j}\right)\big/\bar{a}_{i+1/2,j} \quad && \text{if} \quad \bar{a}_{i+1/2,j} \neq 0 \\ &= 0 && \text{if} \quad \bar{a}_{i+1/2,j} = 0 \end{aligned}$$

(21)

$$\bar{u}_{i,j} = \bar{\mathcal{S}}_w \, \mathrm{Minmod}\left(\left|\bar{w}_{i+1/2,j}\right|, \bar{w}_{i-1/2,j}\,\bar{\mathcal{S}}_w\right)$$

$$\bar{\mathcal{S}}_w = \mathrm{sgn}(\bar{w}_{i+1/2,j})$$

(22)

$$\bar{w}_{i+1/2,j} = \tfrac{1}{2}\left(\mathrm{Abs}(\bar{l}_{i+1/2,j}) - (\bar{l}_{i+1/2,j})^2\right)\bar{a}_{i+1/2,j}$$

(23)

where $\mathrm{Minmod}(x,y) = \max\left[0, \min(x,y)\right]$. The eigenvalues $\bar{\lambda}$ are non-dimensionalized by τ, the ratio of integration time step and local cell spacing,

$$\bar{l}_{i+1/2,j} = \bar{\lambda}_{i+1/2,j} \, \tau_{i+1/2,j}$$

(24)

$$\tau_{i+1/2,j} = \frac{\Delta t \, \Delta A_{i+1/2,j}}{\tfrac{1}{2}\left(\Delta V_{i,j} + \Delta V_{i+1,j}\right)}$$

(25)

$$\bar{\lambda}_{i+1/2,j} = \bar{\lambda}(\bar{Q}^p_{i+1/2,j}) = \begin{bmatrix} v_n - a \\ v_n \\ v_n + a \\ v_n \end{bmatrix}_{i+1/2,j} \tag{26}$$

In all calculations, the flow field is initialized impulsively, i.e. all the fluid cells in the interior computational domain are assigned free stream values. Thereafter, the far-field boundary cells are maintained at the free stream conditions. A no-slip condition is implemented at the solid boundary together with a pressure-density gradient extrapolation based on the adiabatic wall condition.

VII. Computational Results

The 2-D flow over a cylinder was computed at a Mach number $M = 0.3$ and diameter-based Reynolds numbers of $Re = 50, 60, 65, 70, 100, 1000$. For $Re = 50$ and 60, the flow field grew steadily symmetric with two stable vortices. The following observations were made for flow Reynolds numbers of 65 and above: After the mean flow had traveled between 100 to 1000 cylinder diameters from its impulsive and disturbance free beginning, alternate vortex shedding initiated and a periodic von Karman vortex street developed in the wake. The time history of the lift coefficient can be mathematically described in two stages, an exponential growth starting near machine precision, $C_{L,0} \approx 10^{-16}$, followed by periodic oscillation through shedding, where f_L and g_L are the dimensional (1/s) frequency and growth rate,

Growth Stage: $\qquad C_L(t) = C_{L,0} \cdot \sin(2\pi f_L t) \cdot \exp(g_L t)$

$$\tag{27}$$

Shedding Stage: $\qquad C_L(t) = C_{L,\text{amp}} \cdot \sin(2\pi f_L t)$

Both frequency and growth rate can be non-dimensionalized via a frequency f_∞ based on free stream flow speed V_∞ and cylinder diameter D. The flow speed itself can be expressed in terms of Mach number and free stream temperature T_∞,

$$f_\infty = \frac{V_\infty}{D} = \frac{M \, a_\infty}{D} = \frac{M}{D} \sqrt{\gamma R T_\infty} \tag{28}$$

The resulting non-dimensional lift frequency and growth rate shall be starred to distinguish themselves from their dimensional counterparts,

$$f_L^* = f_L / f_\infty = St$$

$$\tag{29}$$

$$g_L^* = g_L / f_\infty$$

The non-dimensional lift frequency f_L^* is commonly referred to in the literature as the Strouhal number (St), named after Vincent Strouhal [1], who first attributed the generation of sound in certain flows to their periodicity in 1878. For 2-D periodic flow over a cylinder, the sound and lift frequencies are identical, and the Strouhal number is generally expressed as a function of Reynolds number, although slightly varying results can be found in the literature. The following empirical relations were stated by Aref et al. [10] based on Reynolds number range,

$$50 < Re < 200: \quad St = 0.2175 - 5.1064 / Re$$

$$\tag{30}$$

$$200 < Re < 2 \times 10^5: \quad St = 0.212 - 2.7 / Re$$

Although the viscous damping was too strong in the current computation for vortex shedding to initiate at Reynolds numbers below 65, for higher Reynolds numbers, the lift frequencies during steady periodic flow agree reasonably well with the above empirical relations. A comparison of Strouhal frequency data is shown in Table 2, together with periodic lift and drag coefficient values.

The data in Table 1 show the non-dimensional lift frequencies during the initial growth period, i.e. prior to vortex shedding, which differ significantly from their corresponding Strouhal numbers in Table 2 for steady periodic flow. However, the lift frequency data in Table 1 agree well with the results published by Crouch et al. [14], which were obtained via a linearized global stability analysis. Reference [14] tries to explain the discrepancy through "finite amplitude effects that are neglected in the linear theory." Based on the results of the current CFD simulation, the difference between lift frequencies during the initial instability growth and the steady periodic flow clearly appears to diverge as the flow Reynolds number increases. At $Re = 1000$, the lift frequency more than triples as periodic vortex shedding sets in, and this frequency shift is clearly visible in the amplitude oscillations of Figure 3.

Crouch et al. [14] further analyze the vertical velocity component of the flow in the wake of the cylinder at $x/D = 2$ and calculate a corresponding non-dimensional growth rate g_v^*. Values for this velocity based growth rate for different Reynolds numbers are listed next to the non-dimensional lift growth rates g_L^* obtained in the current simulation. Needless to say, it is difficult to compare lift and wake velocity data, although they are intricately linked, and thus a scale factor of 2/3 was employed to better show the correlation. Clearly, both columns show a trend of increasing growth rates with increasing Reynolds numbers, which seems intuitive.

Re	$(x/D)_{\text{trans}}$	f_L^*	f_L^* [14]	g_L^*	$\frac{2}{3} g_v^*$ [14]
50	--	0.000	0.116	0.000	0.008
60	--	0.000	0.118	0.000	0.030
65	1015	0.123	0.118	0.035	0.039
70	724	0.124	0.118	0.047	0.046
100	326	0.125	0.114	0.085	0.073
1000	117	0.070	--	0.279	--

Table 1: Transition Travel, Lift Frequency and Growth Rate of Transient Flow, and Comparison with [14]

| Re	$C_{D,\text{ave}}$	$C_{D,\text{amp}}$	$C_{L,\text{amp}}$	$St = f_L^*$	St [10]
50	1.482	0.000	0.000	0.000	0.115
60	1.386	0.000	0.000	0.000	0.132
65	1.418	0.001	0.106	0.135	0.139
70	1.405	0.001	0.133	0.139	0.145
100	1.335	0.004	0.247	0.156	0.166
1000	1.532	0.160	1.365	0.239	0.209

Table 2: Drag, Lift, Lift Frequency (Strouhal Number) of Steady Periodic Flow, and Comparison with [10]

The drag data in Table 2 is split into two separate coefficients for time average mean and periodic peak amplitude. Mathematically, the drag coefficient during the shedding stage can be described as follows,

$$\text{Shedding Stage:} \qquad C_D(t) = C_{D,\text{ave}} + C_{D,\text{amp}} \cdot \sin(2\pi f_D t) \quad \text{where} \qquad f_D = 2 \cdot f_L \qquad (31)$$

The drag reaches a maximum right after the lift has passed through a maximum or minimum. Thus the drag frequency is exactly twice the lift frequency, which becomes clearly evident upon comparison of the periodic portions of Figure 1 and 2. The very small phase difference between lift and drag was neglected in the drag equation.
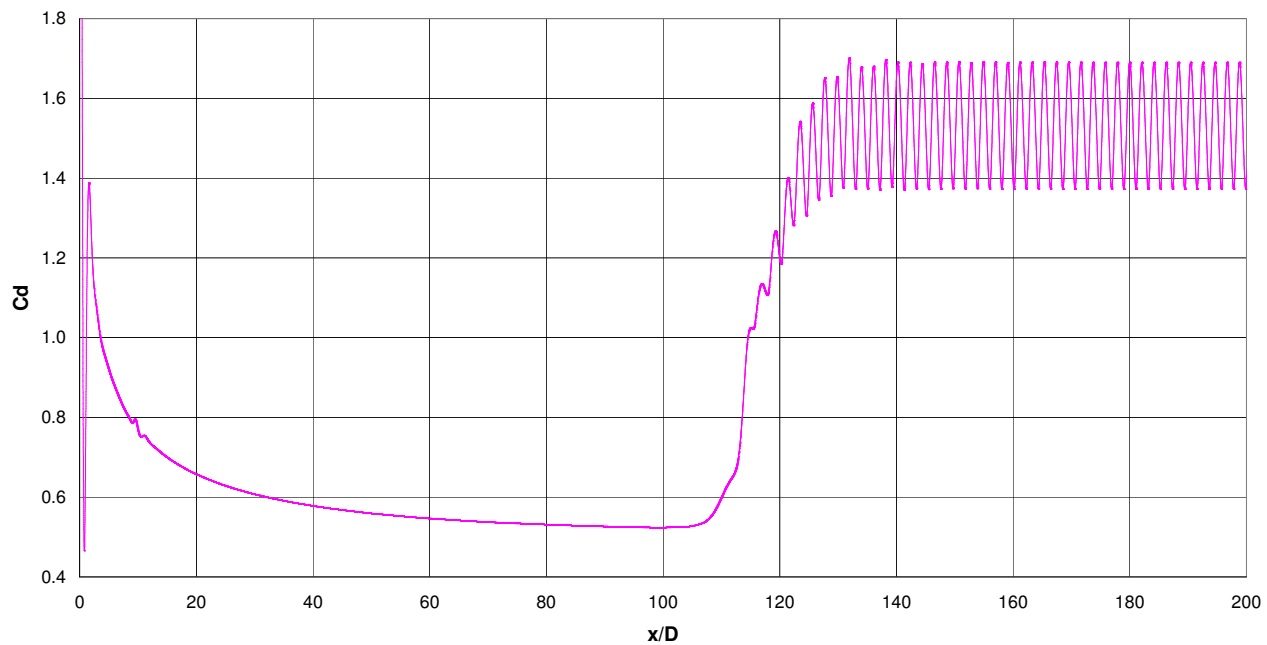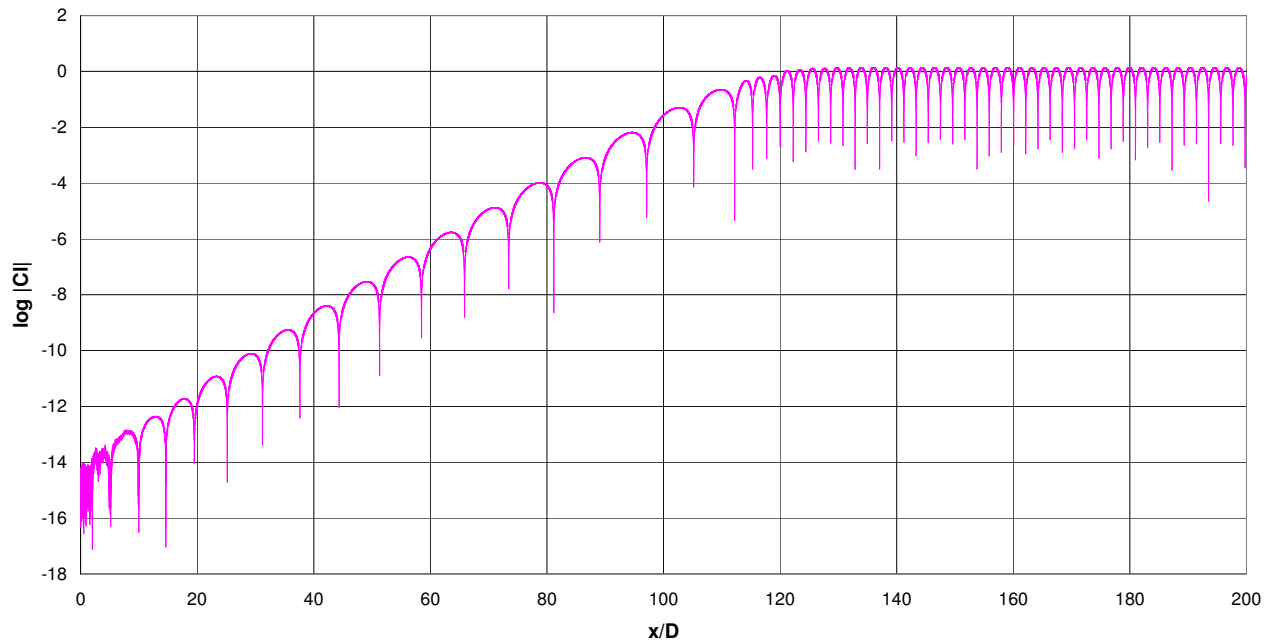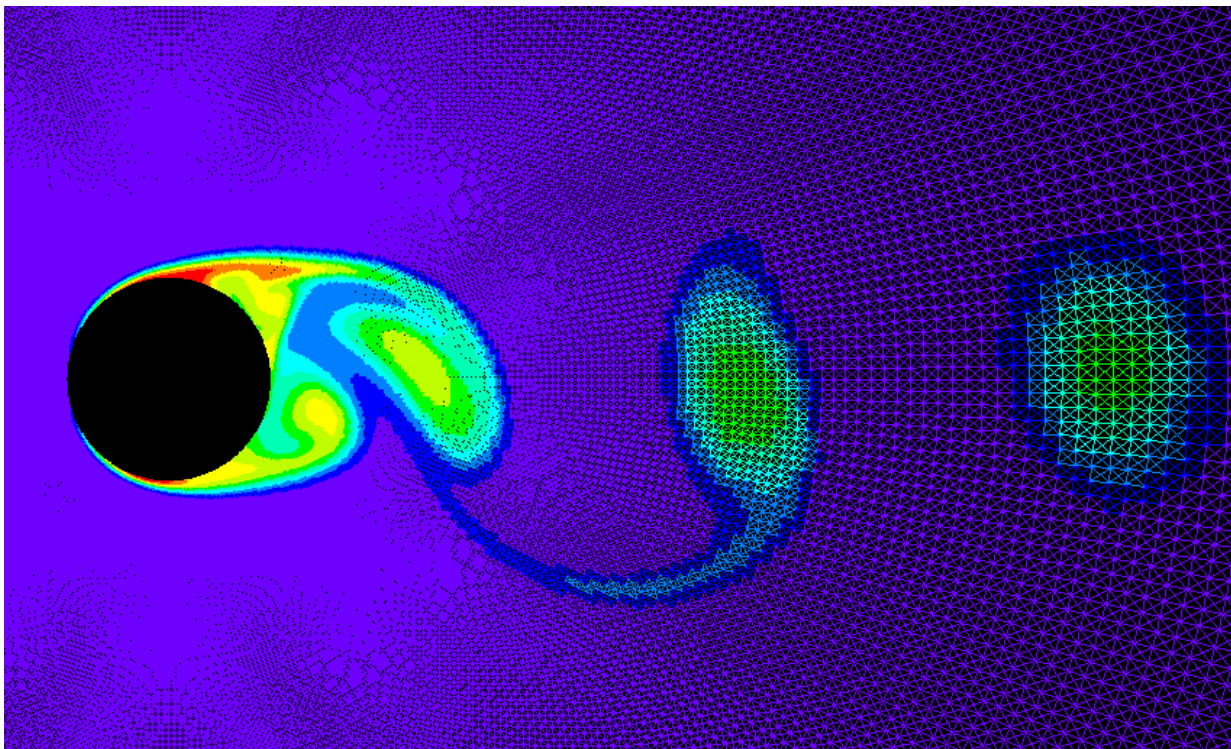
Figure 1: Drag Coefficient versus Cylinder Diameters traveled at $Re = 1000$
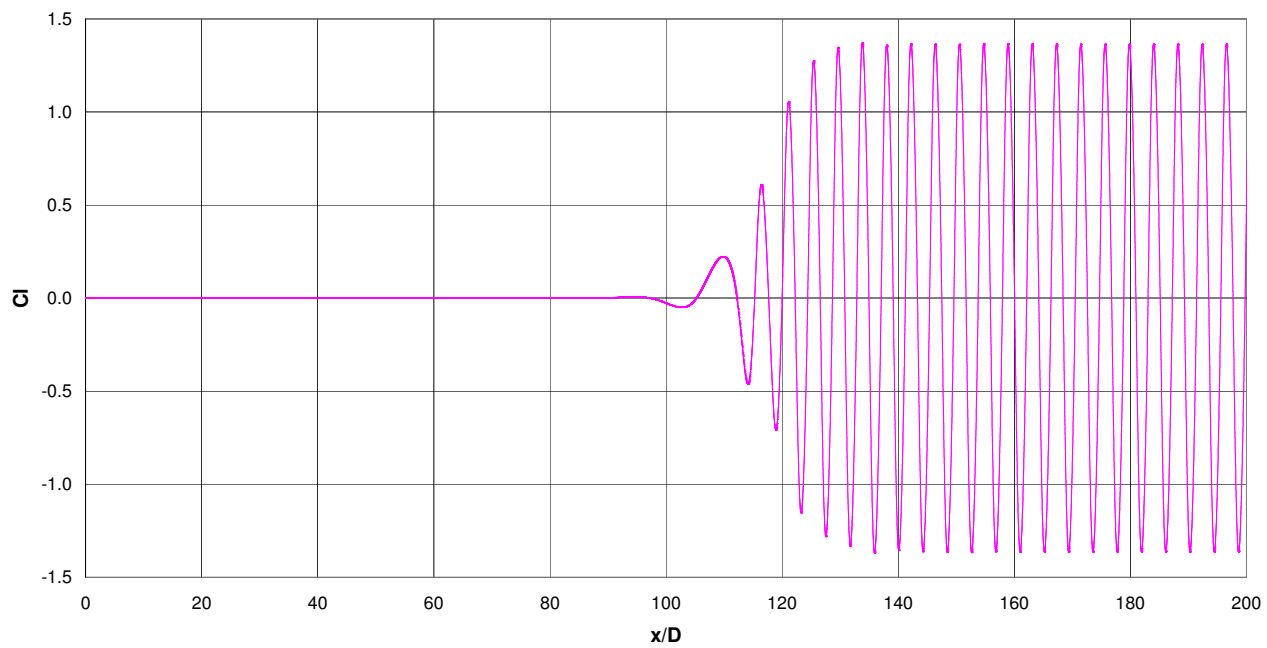
Figure 2: Lift Coefficient versus Cylinder Diameters traveled at $Re = 1000$

American Institute of Aeronautics and Astronautics

Figure 3: Logarithm of Lift Coefficient versus Cylinder Diameters traveled at $Re = 1000$

Figure 4: Mesh and Entropy Plot of Cylinder Wake at $Re = 1000$

American Institute of Aeronautics and Astronautics

During the growth stage of lift, the drag decreases asymptotically and reaches its minimum right before the onset of vortex shedding. For the case presented in Figure 1, at a flow Reynolds number of 1000, the minimum drag coefficient occurs near $x/D = 99$ with $C_{D,\min} = 0.5237$. The average drag coefficient during the subsequent periodic stage reaches nearly three times that value, $C_{D,\mathrm{ave}} = 1.532$. Similar drag histories were observed at lower Reynolds numbers with flow periodicity ($Re = 65, 70, 100$), although the drag difference between pre- and post-vortex shedding was much smaller, only about 5 to 12% of the time averaged mean value.

Mittal [12] published aerodynamic coefficients for 2-D unsteady flow simulations over a cylinder at Reynolds numbers of 50, 100, 200, 300 in terms of time averaged mean and root-mean-square amplitude. Since the periodic wave forms are nearly sinusoidal, Mittal's root-mean-square values can easily be converted to peak amplitude through a multiplication with $\sqrt{2}$; a comparison of calculated and directly quoted value for peak lift at $Re = 100$ was less than 1%. The time averaged drag coefficients at $Re = 50$ and 100 shown in Table 2 compare very well with those published by Mittal, $C_{D,\mathrm{ave}} = 1.416$ and 1.332, respectively. However, Mittal's peak amplitude of lift and drag coefficients at $Re = 100$, $C_{L,\mathrm{amp}} = 0.319$ and $C_{D,\mathrm{amp}} = 0.009$, are significantly different from those in Table 2. Although there is no obvious answer for these amplitude discrepancies, it should be pointed out that Mittal solved the incompressible flow equations ($M = 0$), whereas the present flow solution is marginally compressible ($M = 0.3$).

VIII. Conclusion

The current CFD simulations for 2-D flow over a cylinder show that flow instability can grow from numerically infinitesimal disturbances and that its exponential growth rate is constant until the large scale periodicity of the flow sets in through vortex shedding. The equivalent free stream turbulence intensity of "disturbance free" numerically simulated flow is on the order of machine precision, about 10^{-16} for a 64-bit floating point number representation. The precise value of machine precision, also commonly referred to as machine epsilon or unit round-off, is 1.11×10^{-16} based on the IEEE 745-2008 double precision (64-bit) floating point number format. No matter what bit precision is used though, a numerical wind tunnel, just like its physical counterpart, is never entirely turbulence free.

The applied CFD code was designed for aerospace applications, where flows are generally compressible ($M > 0.3$), and thus it is somewhat limited in serving as a benchmark test tool for incompressible flows ($M = 0$) that are frequently encountered in the literature like the cylinder problem. Nonetheless, the simulation predicted the drag coefficients and dimensionless frequencies (Strouhal numbers) for 2-D cylinder flow with periodic vortex shedding reasonably well compared to values published in the literature. Remarkably, the sudden increase of lift and drag frequency during the onset of vortex shedding at flow Reynolds numbers of 100 and above was very well predicted, a phenomenon that previously divided the results of linear stability theory with those found by experimental and computational studies that did not investigate the exponential growth stage. Thus this research bridges the apparent gap between the frequency predictions of the more recent linearized global stability analyses and the well established results of past experimental and computational studies for 2-D periodic flow over cylinders.

References

[1] Strouhal, Vincent. *Über eine besondere Art der Tonerregung.* Annalen der Physik und Chemie, 1878, Band 241, 216-251.
[2] Rayleigh, John William Strutt, Baron. *Acoustical observations.* Philosophical Magazine, 1879, 5th Series, Volume 7, 149-162.
[3] Von Karman, Theodor, and H.L. Rubach. *Über den Mechanismus des Flüssigkeits- und Luftwiderstandes.* Physikalische Zeitschrift, 1912, Band 13, 49-59.

[4] Swanson, J.C., and M.L. Spaulding. *Three dimensional numerical model of vortex shedding from a circular cylinder*. Nonsteady Fluid Dynamics, ASME Winter Annual Meeting, San Francisco, 1978, 207-216.

[5] Braza, M., P. Chassaing, and H. Ha Minh. *Numerical study and physical analysis of the pressure and velocity fields in the near wake of a circular cylinder*. Journal of Fluid Mechanics, 1986, Volume 165, 79-130.

[6] Henderson, Ronald D., and Dwight Barkley. *Secondary instability in the wake of a circular cylinder*. Physics of Fluids, 1996, Volume 8, Number 6, 1683-1685.

[7] Rocchi, D., and A. Zasso. *Vortex shedding from a circular cylinder in a smooth and wired configuration: comparison between 3D LES simulation and experimental analysis*. Fourth International Colloquium on Bluff Body Aerodynamics & Applications, Bochum, Germany, 2000, 479-482.

[8] Siegel, Stefan, Kelly Cohen, and Thomas McLaughlin. *Numerical Simulations of a Feedback-Controlled Circular Cylinder Wake*. AIAA Journal, 2006, Volume 44, Number 6, 1266-1276.

[9] Spiker, Meredith A., J.P. Thomas, K.C. Hall, R.E. Kielb, and E.H. Dowell. *Modeling Cylinder Flow Vortex Shedding with Enforced Motion Using a Harmonic Balance Approach*. AIAA Paper 2006-1965, 2006.

[10] Aref, H., M. Brøns, and M.A. Stremler. *Bifurcation and instability problems in vortex wakes*. Journal of Physics, 2007, Conference Series 64, 012015, 1-14.

[11] Singh, S.P., and S. Mittal. *Flow past a cylinder: shear layer instability and drag crisis*. International Journal for Numerical Methods in Fluids, 2005, Volume 47, 75-98.

[12] Mittal, Sanjay. *Excitation of shear layer instability in flow past a cylinder at low Reynolds number*. International Journal for Numerical Methods in Fluids, 2005, Volume 49, 1147-1167

[13] Mittal, Sanjay. *Instability of the separated shear layer in flow past a cylinder: Forced excitation*. International Journal for Numerical Methods in Fluids, 2008, Volume 56, 687-702.

[14] Crouch, J.D., A. Garbaruk, and D. Magidov. *Predicting the onset of flow unsteadiness based on global instability*. Journal of Computational Physics, 2007, Volume 224, 924-940.

[15] Provansal, M., C. Mathis, and L. Boyer. *Benard-von Karman instability: transient and forced regimes*. Journal of Fluid Mechanics, 1987, Volume 182, 1-22.

[16] Harten, Ami. *High Resolution Schemes for Hyperbolic Conservation Laws*. Journal of Computational Physics, 1983, Volume 49, 357-393.

[17] Yee, H.C., and P. Kutler. *Application of Second-Order-Accurate TVD Schemes to the Euler Equations in General Geometries*. NASA Technical Memorandum, TM 85845, 1983.

[18] Yee, H.C., R.F. Warming, and Ami Harten. *"On a Class of TVD Schemes for Gas Dynamic Calculations", Numerical Methods of the Euler Equations of Fluid Dynamics*. Edited by F. Angrand, A. Dervieux, J.A. Desideri, and R. Glowinski. Society for Industrial and Applied Mathematics, Philadelphia, PA, 1985, 84-107.

[19] Wang, J.C.T., and G.F. Widhopf. *A High-Resolution TVD Finite Volume Scheme for the Euler Equations in Conservation Form*. Journal of Computational Physics, 1989, Volume 84, 145-173.

[20] Wang, Z., and B.E. Richards. *High Resolution Schemes for Steady Flow Computation*. Journal of Computational Physics, 1991, Volume 97, 53-72.

[21] Lu, Pong-Jeu, and Kuen-Chuan Wu. *Assessment of TVD Schemes in Compressible Mixing Flow Computations*. AIAA Journal, 1992, Volume 30, Number 4, 939-946.

[22] Smithwick, Quinn, and Scott Eberhardt. *Fuzzy Controller and Neuron Models of Harten's Second-Order TVD Scheme*. AIAA Journal, 1994, Volume 32, Number 10, 2122-2124.

[23] Jeng, Yih Nen, and Uon Jan Payne. *An Adaptive TVD Limiter*. Journal of Computational Physics, 1995, Volume 118, 229-241.

[24] Li, X.L., B.X. Jin, and J. Glimm. *Numerical Study for the Three-Dimensional Rayleigh-Taylor Instability through the TVD/AC Scheme and Parallel Computation*. Journal of Computational Physics, 1996, Volume 126, 343-355.

[25] Rohde, Axel. *A Computational Study of Flow Around a Rotating Disc in Flight*. Dissertation in Aerospace Engineering, Florida Institute of Technology, 2000. Published via the author's website, www.microcfd.com.